



Improving Electrochemical Activity of P2-type $\text{Na}_{2/3}\text{Mn}_{2/3}\text{Ni}_{1/3}\text{O}_2$ by Controlling its Crystallinity

Riki Kataoka,^{*[a]} Noboru Taguchi,^[a] Kohei Tada,^[a] Akihiko Machida,^[b] and Nobuhiko Takeichi^[a]

Layered P2-type Na containing manganese-nickel oxide ($\text{Na}_{2/3}(\text{Mn}_{2/3}\text{Ni}_{1/3})\text{O}_2$) materials show relatively higher electrochemical capacity. The electrochemical performance of $\text{Na}_{2/3}(\text{Mn}_{2/3}\text{Ni}_{1/3})\text{O}_2$ decreases during cycling when more than 1/2 of Na was extracted owing to the structural change with large volume change and oxygen emission. We found that smaller crystallite size and introduction of the defects at transition metal site of $\text{Na}_{2/3}(\text{Mn}_{2/3}\text{Ni}_{1/3})\text{O}_2$ plays a key role to improve its cycling performance. The structural analysis observations using X-ray total scattering analysis, X-ray absorption fine structure (XAFS) and transmission electron microscopy (TEM), revealed that the

length and numbers of stacks of the MO_2 layers were shortened and decreased, respectively, compared to that of P2-type layered $\text{Na}_{2/3}(\text{Mn}_{2/3}\text{Ni}_{1/3})\text{O}_2$. This short-range ordering of the layered structure restricts the structural change during cycling resulting in mitigating large volume changes. Moreover, the metal defects at the transition metal site of the $\text{Na}_{2/3}(\text{Mn}_{2/3}\text{Ni}_{1/3})\text{O}_2$ increases the contribution of the oxygen redox which confirmed by the density functional theory calculation, without showing significant overpotential and capacity fading during cycling.

Introduction

Sodium-ion batteries have been regarded as cost effective and sustainable energy storage systems owing to the low cost and wide distribution of Na resources. A battery's performance and cost are mainly determined by the cathode materials used. A wide range of positive electrode materials have been reported, including layered oxide materials, polyanion-types and Prussian-analogs. The sodium (Na) containing layered transition metal (TM) oxide materials can be synthesized easily and have high capacity, making them the most extensively studied materials. Two types of layered oxide materials have been identified, as Delmas first classified:^[1] the O3 type, in which the Na ions reside in octahedral sites with oxygen coordination and the P2-type, in which the Na ions occupy the trigonal prismatic sites. In contrast to the O3 type structures, the P2-type structure has smoother Na ion diffusion pathways, which has high-rate capability, along with a higher redox potential.^[2] In addition, $\text{Na}_{2/3}(\text{Mn}_{2/3}\text{Ni}_{1/3})\text{O}_2$ with P2-type layered oxide material is an attractive material, with low minor element composition, 160 mAh g⁻¹ theoretical capacity and high working potential over 3.7 V, which are comparable to those of the positive electrode materials of lithium ion battery.^[3] The Mn ion in $\text{Na}_{2/3}$

$(\text{Mn}_{2/3}\text{Ni}_{1/3})\text{O}_2$ material maintains tetravalent coordinates during redox, therefore this material is not affected by Jahn-Teller distortion of trivalent Mn ion which affects electrochemical performance of the active materials. However, the P2 structure exhibits rapid decay of capacity owing to the structural change to the O2/OP4 structure at higher state of charge. In addition to such the change in the stacking order of layers changes as a result of gliding of the TM oxide layers, the emission of oxygen at the end of charge further causes irreversible structural changes.^[4,5] To mitigate these structural changes, different metal substitutions have been investigated and were found to improve the cycling performance of P2- $\text{Na}_{2/3}(\text{Mn}_{2/3}\text{Ni}_{1/3})\text{O}_2$.^[6-8] Moreover, some of the substituents, such as Mg, Li, and the introduction of the vacancy at the TM sites facilitate the oxygen redox activity in layered Na_xMO_2 materials^[9-17] by generating the nonbonding oxygen orbits along Na-O-X configurations, where X represents Li, Mg or vacancy.

Herein, we focus on the crystallinity of the layered structure to improve the electrochemical property of P2-type $\text{Na}_{2/3}(\text{Mn}_{2/3}\text{Ni}_{1/3})\text{O}_2$ in contrast to aforementioned approaches that concentrated on metal substitutions. As shown in Figure 1, a well crystallized material glides easily between the layers, whereas in the case of less crystalline materials, the crystallites tend to agglomerate into small crystal, resulting in an increase in interfaces (grain boundaries), which would interfere with layer gliding and restrict structural changes. The effect of crystallite size plays an important role in high pressure studies, for example, the high pressure transition of nano ZrO_2 , whose crystallite size is less than 30 nm, starts approximately three times (3 GPa) higher compared to that of the transition of ZrO_2 with a crystallite size greater than 100 nm.^[18] For battery materials, nano sizing have been reported to restrict O3-P3 phase transition during charge and discharge.^[19]

In this study, the effect of crystallinity on the electrochemical property of the P2- $\text{Na}_{2/3}(\text{Mn}_{2/3}\text{Ni}_{1/3})\text{O}_2$ was explored

[a] Dr. R. Kataoka, Dr. N. Taguchi, Dr. K. Tada, Dr. N. Takeichi
Research Institute of Electrochemical Energy,
Department of Energy and Environment
National Institute of Advanced Industrial Science and Technology (AIST)
1-8-31 Midorigaoka, Ikeda, Osaka, 563-8577 (Japan)
E-mail :
E-mail: riki-kataoka@aist.go.jp

[b] Dr. A. Machida
Synchrotron Radiation Research Center
National Institutes for Quantum Science and Technology(QST)
Sayo Hyogo 679-5148 (Japan)

 Supporting information for this article is available on the WWW under
<https://doi.org/10.1002/batt.202200462>

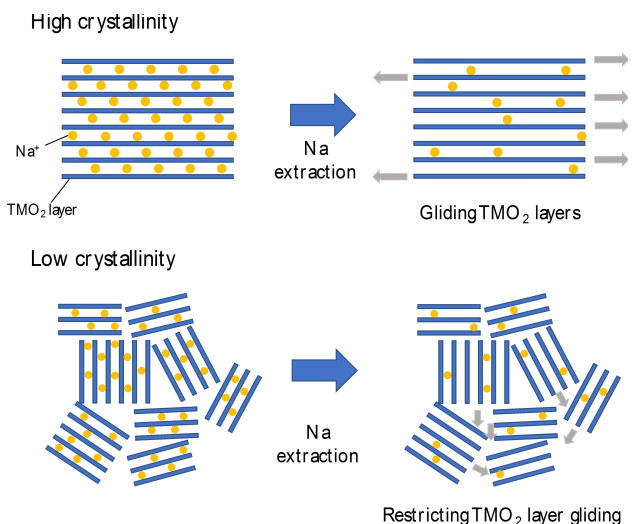


Figure 1. Schematic diagrams of the layer gliding mechanism of the well crystallized (high crystallinity) and the disordered (low crystallinity) structure.

using the ball milling approach. The electrochemical property of $\text{Na}_{2/3}(\text{Mn}_{2/3}\text{Ni}_{1/3})\text{O}_2$, with lower crystallinity prepared by the mechanical milling process, was evaluated. Structural analysis using the synchrotron X-ray total scattering measurement, X-ray absorption spectroscopy (XAS) and transmission electron microscopy (TEM) revealed that the milled $\text{Na}_{2/3}(\text{Mn}_{2/3}\text{Ni}_{1/3})\text{O}_2$ sample shows short-range layered ordering in several nm order crystallites and contains vacancies at TM sites. In addition, the charge compensation mechanism using XAFS analysis showed that the oxygen orbital contributed to redox reaction at higher state of charge.

Results and Discussion

Characterization

Figure 2 shows XRD patterns of as-sintered and milled $\text{Na}_{2/3}(\text{Mn}_{2/3}\text{Ni}_{1/3})\text{O}_2$ samples at 500 rpm for 2 and 10 h, respectively. The pattern of the as-sintered sample could be identified as the P2-type hexagonal layered structure (space group $P6_3/mmc$,

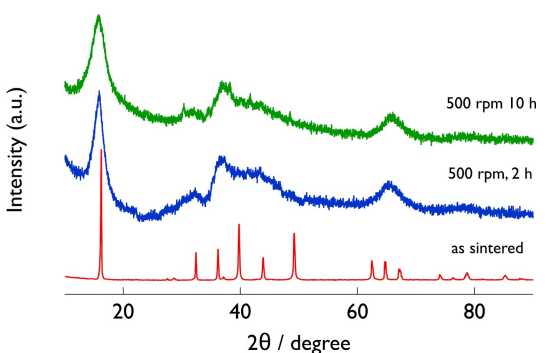


Figure 2. XRD patterns of as-sintered and milled at 500 rpm for 2 h and 10 h of $\text{Na}_{2/3}(\text{Mn}_{2/3}\text{Ni}_{1/3})\text{O}_2$ samples.

No. 194). The electrochemical performance may be affected by a trace amount of impurity phase, approximately 5 wt.% NiO phase, but the effect was considered to be limited.

The occupancy of the Na ion, which was refined by Rietveld method, was found to be 0.717, which was in good agreement with ICP result ($\text{Na}/\text{M} = 0.66$). The result of Rietveld refinement and other refined structural parameters are summarized in Figure S2 and Table S1. The XRD pattern of the sample milled for 2–10 h showed a number of diffracted peaks, which disappeared and/or broadened, indicating that ball milling lowered the crystallinity and structural symmetry of the sample. Also, although some new peaks appeared suggesting new phase, the detailed crystal structure of the milled samples cannot be determined by XRD analysis. However, the peak around 16° – 17° , which reflects the layered structure of the material, was clearly confirmed. As reported in previous studies, the mechanical milling process causes Na (or Li) transition-metal cation mixing of layered structure, yielding a cation disordered rock salt (NaCl) structure.^[20,21] The NaCl structure, however, was not confirmed in $\text{Na}_{2/3}(\text{Mn}_{2/3}\text{Ni}_{1/3})\text{O}_2$ sample, which was milled for a longer time as shown in Figure 2, suggesting that ball milling does not cause the Na-TM cation mixing. A milling speed higher than the one used in the present study may be able to prepare the cation disordered NaCl phase. The two milled sample not only showed similar XRD patterns but also electrochemical performance, therefore, we will show the results of the sample milled for 2 h and discuss the detailed structural and electrochemical properties comparing to the sintered sample.

Figure 3 shows reduced PDFs, $G(r)$, of the as-sintered sample and the 2 h milled sample in the r range of 0.1–1.0 nm and 0.1–2.0 nm, respectively. The simulated PDF patterns of the P2- $\text{Na}_{2/3}(\text{Mn}_{2/3}\text{Ni}_{1/3})\text{O}_2$ and the NaCl type cation disordered structure are also shown in Figure 2. The structural parameters for the simulation of P2-type were used in Table S1. The PDF pattern of NaCl type structure was simulated using the structural parameter of NaCl type cation disordered NaMnO_2 .^[22] Experimental PDF pattern of the as-sintered sample was similar to the simulated pattern of the P2-type structure. The as-sintered sample showed additional peaks compared to that of simulated P2-type structure owing to the presence of conductive additive and PTFE. The PDF pattern of the milled sample was similar to that of the as-sintered sample in the short range between 0.1–1.0 nm, indicating the locally P2-type ordering in the structure of the milled sample. The simulated pattern of the cation disordered NaCl-type structure was different from that of milled sample as described in the XRD results indicating that milled sample contains cation disordered NaCl phase. The signal intensity of milled sample decayed rapidly in the r range greater than 1.0 nm unlike that of sintered one, indicating that layer ordering of milled sample was limited in the short range. Some new peaks observed in XRD profile of the milled sample suggests new structural ordering but based on this PDF results, milled sample would have the P2-type structural ordering in the short range.

Figure 4 shows comparison of the extended X-ray absorption fine structure (EXAFS) spectrum for as-sintered and milled

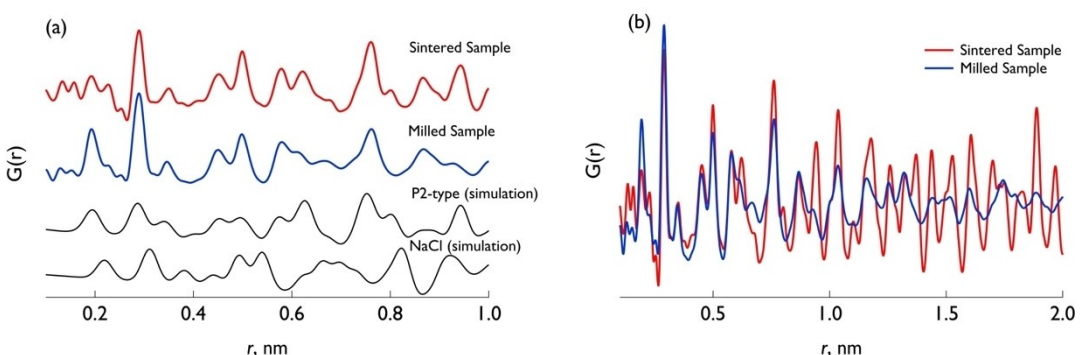


Figure 3. Reduced pair distribution function profiles of as-sintered and milled for 2 h samples in the r range of a) 0.1–1.0 nm and b) 0.1–2.0 nm. The simulated PDF profiles of P2 type layered structure and cation disordered NaCl-type structure were shown in (a) for comparison.

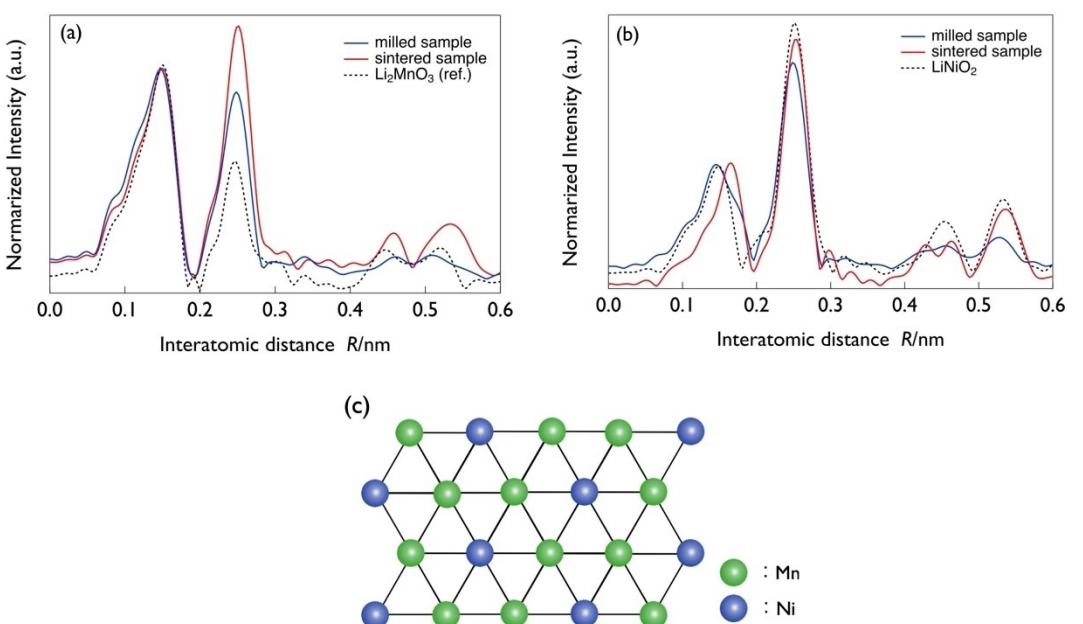


Figure 4. Magnitude of Fourier transformed EXAFS as a function of distance from a) the Mn atoms and b) Ni atoms. c) Atomic ordering of Mn and Ni in the transition metal layer of the $\text{P2}-\text{Na}_{2/3}(\text{Mn}_{2/3}\text{Ni}_{1/3})\text{O}_2$.

samples as functions of atomic distance from Mn and Ni atoms. In the $\text{P2}-\text{Na}_{2/3}(\text{Mn}_{2/3}\text{Ni}_{1/3})\text{O}_2$ structure, Mn and Ni atoms were in regular order in the TM layer, as shown in Figure 4(c), such that the local structures surrounding Mn and Ni were different. The TM layer was ordered in such a way that each Mn was surrounded by three Mn and three Ni atoms, whereas each Ni was surrounded by six Mn atoms.

The first and second peaks were assigned to TM–O and TM–TM interactions, respectively, including Mn and Ni. In Figure 4(a), Comparing the second peak intensities of the samples, the second peak intensity of the milled sample was obviously lower than that of the as-sintered sample but higher than that of Li_2MnO_3 , which was used as a reference. The peak intensity of EXAFS reflects on the coordination numbers of center atom. Mn atom in the TM layer of Li_2MnO_3 was surrounded by three Mn atoms and three Li atoms,^[23] resulting in significantly weak second peak of Li_2MnO_3 because Li was not detected by the X-

ray radiation. Since the peak intensity of EXAFS reflects on the coordination number of center atom, the Mn ion in the milled sample would be surrounded by 3–6 TMs, i.e., some defects were generated at the Mn or Ni site during ball milling. Alternatively, the intensities of the second peak in EXAFS spectrum of Ni K-edge were approximately the same for both the as-sintered and LiNiO_2 sample (in which Ni was surrounded by 6 TMs) and was slightly lower for the milled sample as shown in Figure 4(b), suggesting that the generation of the defects at Mn site surrounding the Ni atoms were unlikely.

The decrease in the intensity of the Mn-TM(Mn and Ni) correlations was more pronounced than that of the Ni-TM (only Mn) correlations, suggesting that more defects were generated around the Ni site.

Figure 5 shows SEM images of as-sintered and milled sample. The as-sintered sample was well-sintered and the primary particle size of the sample was roughly more than 1 μm , which agglomerates to form secondary particles about

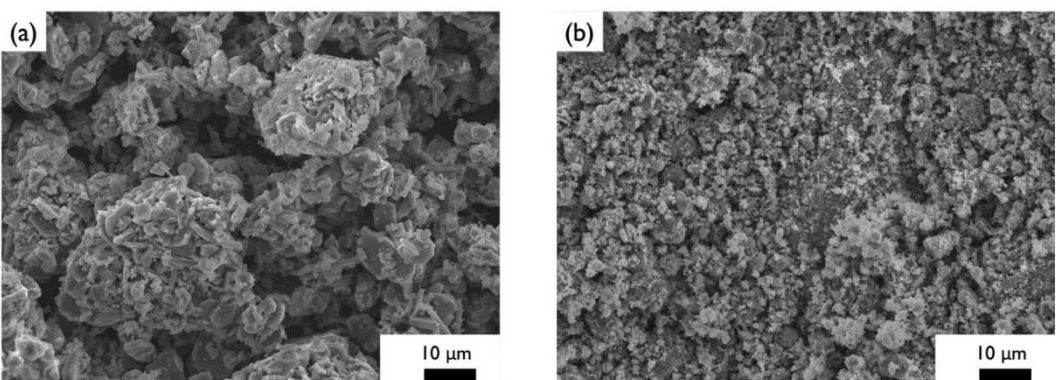


Figure 5. SEM images of a) as-sintered and b) milled sample.

more than 10 μm . The particle size of milled sample, on the other hand, was less than 1 μm due to the mechanical milling process.

Figure 6 shows TEM images of (a) as-sintered and (b) milled sample. The P2-type stacking structure was confirmed in the atomic resolution owing to the well ordered structure of the as-sintered sample. Inter layer distance of TM oxides was evaluated to be 0.55 nm corresponding to the value calculated from XRD result.

Although the milled $\text{Na}_{2/3}(\text{Mn}_{2/3}\text{Ni}_{1/3})\text{O}_2$ samples did not show clear layering, several piles of stacking structures in very short range of several nm order were observed as shown in Figure 6(b). The detailed electrochemical properties of both as-sintered and milled samples have been compared in the following section.

Electrochemical property

Figure 7 shows the charge and discharge curves of as-sintered, milled $\text{Na}_{2/3}(\text{Mn}_{2/3}\text{Ni}_{1/3})\text{O}_2$ samples and their cycling performance tested in the potential range between 2.5 and 4.5 V (vs. Na^+/Na) at a current density of 10 mA g^{-1} . The charge and

discharge profiles of as-sintered sample have three plateaus at 3.1–3.3, 3.5–3.7 and 4.1–4.3 V (vs. Na^+/Na), respectively. The two plateaus at lower and that at higher potentials were observed owing to the change in Na ordering and stack ordering, from P2 to O2 structural change.^[24] The initial charge and discharge capacities of sintered $\text{Na}_{2/3}(\text{Mn}_{2/3}\text{Ni}_{1/3})\text{O}_2$ sample were 175 and 146 mAh g^{-1} but decayed rapidly to less than half of its initial capacity in 20 cycles owing to the large volume change accompanied by the P2-O2 structural change occurring at 4.1–4.3 V (vs. Na^+/Na), and the irreversible oxygen emission at the end of charge as reported in many papers.^[8,24–27]

Contrary to the as-sintered sample, the initial charge and discharge capacities of the milled sample were 146 and 141 mAh g^{-1} , respectively, which were relatively lower than that of as-sintered sample. However, the cycling stability improved to a large extent with 85% of initial capacity remaining even after 50 cycles. The Coulombic efficiency of the milled sample was 96% at initial cycle and kept 99% after 10 cycles and that of as-sintered sample was 83% (1st) and kept 97% after 10 cycle, indicating that the milled sample showed good reversibility. No obvious plateaus were observed from the curves of milled sample suggesting that milled sample did not experience any change in the Na orders and stacking order. The

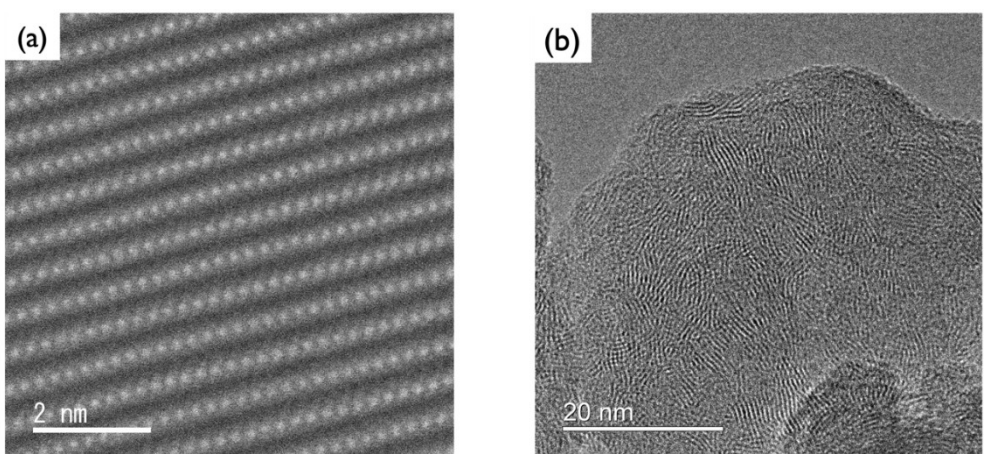


Figure 6. TEM images of a) as-sintered sample (scanning TEM mode) and b) milled sample.

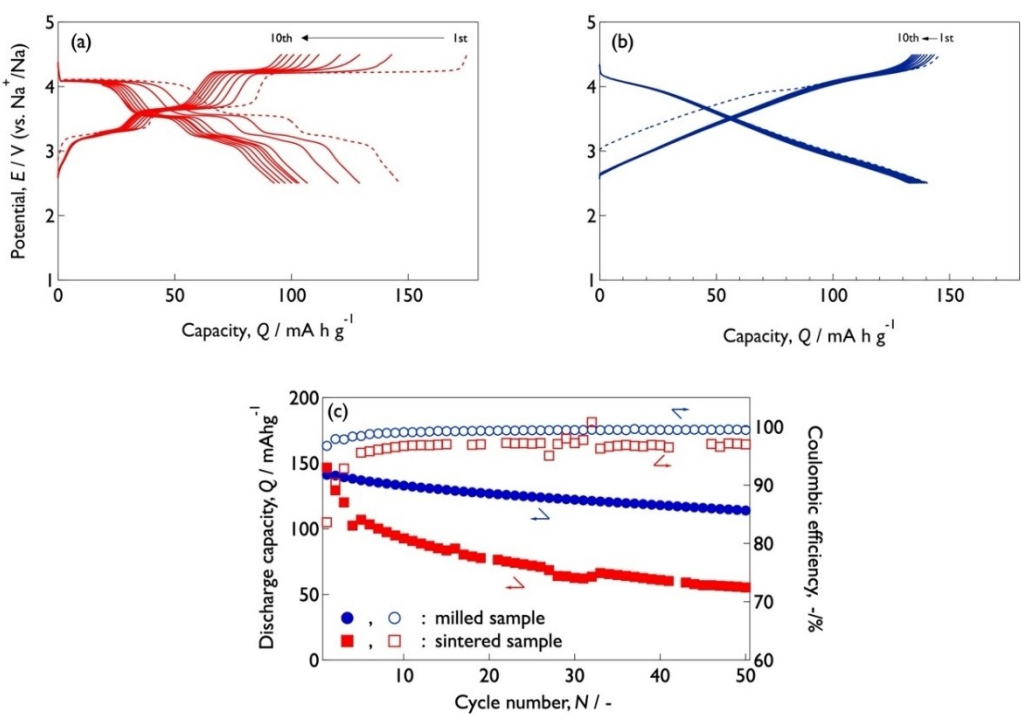


Figure 7. Charge and discharge curves of a) sintered, b) milled samples and c) their cycling performances and Coulombic efficiencies.

reduced PDFs of the milled samples after charge (4.5 V) and discharge (2.5 V) showed similar profile to that before the electrochemical test, Figure S3. Slight peaks shift was confirmed, i.e., interatomic distance contracted/expanded on charging / discharging but no new peaks were detected from the charged and discharged samples. This indicates that the milled sample did not show the structural change, such as P2 to O2 phase transformation, during charge and discharge process.

The average discharge potential of milled sample with value 3.40 V (vs. Na⁺/Na), was lower than that of as-sintered sample, with value 3.68 V (vs. Na⁺/Na), but relatively higher than other reported layered oxide materials.^[28]

The extracted and inserted Na ion estimated from the electrochemical capacity was 0.56 and 0.55, respectively while only less than 0.1 mol Na remained in the host structure. Although the electrochemical performance of layered oxide materials deteriorated significantly when almost all the alkali ions were extracted from the layered oxide material, it was noteworthy that the milled sample showed good cycling performance. Except for a few reports, little is known about the impact of crystallinity on the electrochemical performance of Na-containing layered oxides.^[19] In the case of Li containing layered TM oxide materials, such as LiCoO₂, mechanical milling causes Li-TM cation mixing in layered TM oxide materials containing Li that reduces the electrochemical performance except for LiMnO₂^[22] and layered materials with excess Li, such as Li₂MnO₃.^[21,29] However, in case of Na containing materials, controlling the crystallinity paves way for a new approach for designing materials with better electrochemical performance.

In addition, 1/3 mol Na ion can be further inserted into P2-_{2/3}(Mn_{2/3}Ni_{1/3})O₂ its cycling performance declines and redox potential rapidly decays owing to Jahn-Teller distortion caused by the reduction of tetravalent Mn ion to trivalent ion. However, the decay capacity and redox potential of milled sample was gradual, as shown in Figure S4, indicating that the smaller crystallite size and lattice defects introduced by mechanical milling would be alleviated the structural distortion owing to Jahn-Teller distortion.

In the next section, we will discuss about the significant improvement in cycling performance owing to the restriction of structural change.

Charge and discharge changes in electric state

Firstly, the initial electric structure of both as-sintered and milled samples were compared by the soft XAS measurement. Figure 8 shows Mn, Ni L-edge and O K-edge ex situ XAS spectrum of both sintered (dashed lines) and milled (solid lines) samples during charge and discharge. The O K-edge spectrum in the wide range spectrum was shown in Figure S5. The reference spectrum at the bottom were Li₂Mn⁴⁺O₃ (Figure 8a), NiO (dashed) and LiNiO₂ (solid) (Figure 8b). The points collected in the XAFS spectrum are indicated in Figure 8(d).

The Mn L-edge spectra for pristine samples were similar to that of Li₂Mn⁴⁺O₃ indicating that the Mn ions was tetravalent, and the as-sintered sample was in good agreement with the previous reports. In addition, the Ni L-edge spectra for as-sintered sample was similar to that of NiO indicating that Ni ions in as-sintered sample was divalent, respectively. On the

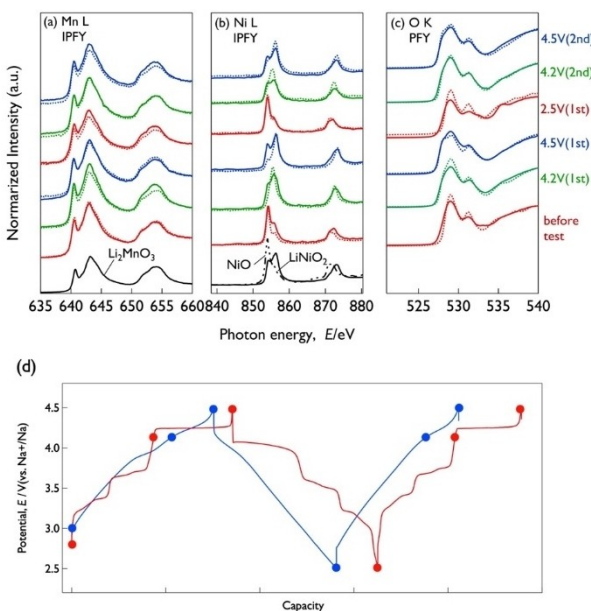


Figure 8. a) Mn and b) Ni L-edge and c) O K-edge ex situ Synchrotron XAS profiles of samples during charge and discharge. d) Charge and discharge curves of sintered and milled samples in the potential range between 2.5 and 4.5 V (vs. Na^+/Na). The plots in the curves indicate the points that XAFS spectrum collected.

other hand, valence state of Ni ion for the milled sample, appeared to be different from that of as-sintered sample. Comparing Ni spectrum in the energy range between 850 and 860 eV of two samples, it was observed that the peak intensity at 856 eV of milled one was larger than that of as-sintered one.

The peak intensity increases when the Ni ion was oxidized from divalent to higher valence state, indicating that the Ni ion in the milled sample was at higher oxidation state compared to that of as-sintered one. As already described, the structural defect at the TM (mainly Ni) site was introduced by the milling process, which would lead to the oxidation of the TM. Oxidation of the tetravalent Mn ion needs a large amount of energy, therefore, only Ni ion would be oxidized on charging to maintain the electroneutrality. Regarding O K-edge spectrum, shoulder peak at the lower energy of the pre-edge peak was observed only for the milled sample. The increase in the intensity of shoulder for the milled sample is owing to the formation of hole in the 3d-O 2p hybridization orbital of TM and the hole formation was influenced by the oxidation of Ni ion as confirmed from Ni L-edge XAS.

During charge and discharge, Mn L-edge profiles of both sintered and milled samples remain unchanged, and were redox inactive in the potential range between 2.5–4.5 V (vs. Na^+/Na). The evolution of Ni L-edge profiles differ from each other. The peaks for as-sintered sample around 855 eV, shown by the dashed lines in Figure 8 (b), shifted gradually to higher energy. The charge capacities of as-sintered sample (red line in Figure 7d) were 89 mAh g^{-1} (4.2 V vs. Na^+/Na) and 170 mAh g^{-1} (4.5 V vs. Na^+/Na), corresponding to 0.34 and 0.67 Na^+ equivalent mol extraction, respectively. The Mn ion was redox inactive in this material; therefore, Ni ion would be dominantly

oxidized followed by Na ion extraction. Accordingly, Ni ion would be charged from divalent to trivalent at 4.2 V, and to tetravalent at 4.5 V, assuming that all the electrochemical capacities are consumed by the oxidation of the Ni ion. The peak of Ni L3-edge spectra of as-sintered sample shifted from 854 to 855.4 eV (4.2 V vs. Na^+/Na) and 856.4 eV (4.5 V vs. Na^+/Na), representing divalent, trivalent and tetravalent states, respectively, according to electronic state of $\text{Li}_{1-x}\text{Ni}_{0.5}\text{Mn}_{1.5}\text{O}_4$.^[30] The shape Ni L-edge spectra at 4.2 V of sintered sample differs from that of $\text{LiNi}^{3+}\text{O}_2$, shown at the bottom in Figure 7(b), probably due to the difference in the electronic structure. The Ni ion in the as-sintered sample was oxidized in the same manner during second charge. Regarding milled sample, the peak at higher energy increased during charging to 4.2 V (vs. Na^+/Na) and that is similar to that of the LiNiO_2 . On further charging to 4.5 V (vs. Na^+/Na), the ratio of the peak at 854 eV to that at 856 eV was unaffected or slightly decreased suggesting that Ni ion was not oxidized or rather reduced during further charging. The charged capacity of milled sample was 146 mAh g^{-1} , as stated earlier, and Ni ion would be charged to 3.7+ assuming that only Ni ion compensates electrical charge neutrality. The valence number of Ni ion was estimated to be approximately 3.3 based on the peaks ratios, 854 (Ni^{2+}) and 856.4($^{4+}$) eV, of the sample spectra charged to 4.5 V (vs. Na^+/Na). This estimation may contain errors, however, an additional redox active element, oxygen, should contribute to the charge compensation. The redox reversibility of Ni ion during cycling was confirmed in the milled as well as sintered sample.

A similar behavior was observed when compared with the evolution of O K-edge spectrum of both as-sintered and milled samples as shown in Figure 8(c). The intensity of the shoulder on the lower energy side of the pre-edge peak at 528 eV became larger with increase in state of charge. As already described, when the TM ion or O ion was charged, the pre-edge shoulder appeared indicating that electron was extracted from the hybrid state of TM 3d and O 2p orbitals (σ bonding).^[31] For milled sample, charged from 4.2 V (vs. Na^+/Na) to 4.5 V (vs. Na^+/Na), the intensity of the shoulder appeared to increase although valence number of the Ni ion hardly change (or decrease) in this SOC range as confirmed by Ni L-edge XAS spectrum. Therefore, the increase in the pre-edge at 528 eV owing to the oxidation of O^{2-} ion for the charge compensation. This indicates that the lowering the crystallinity of $\text{Na}_{2/3}(\text{Mn}_{2/3}\text{Ni}_{1/3})\text{O}_2$ made the oxide ion easier to redox during sodium insertion and extraction process. It is worth noting that the electrode material that utilizes oxygen redox for charge compensation shows good cycling performance. The origin of the oxygen redox has been discussed in the next section.

Theoretical calculation

In the previous section, the oxygen redox was confirmed in the sample with lower crystallinity (milled sample). The defects at metal site, dominantly Ni sites would affect the oxygen redox in the milled sample. Therefore, DFT calculations were

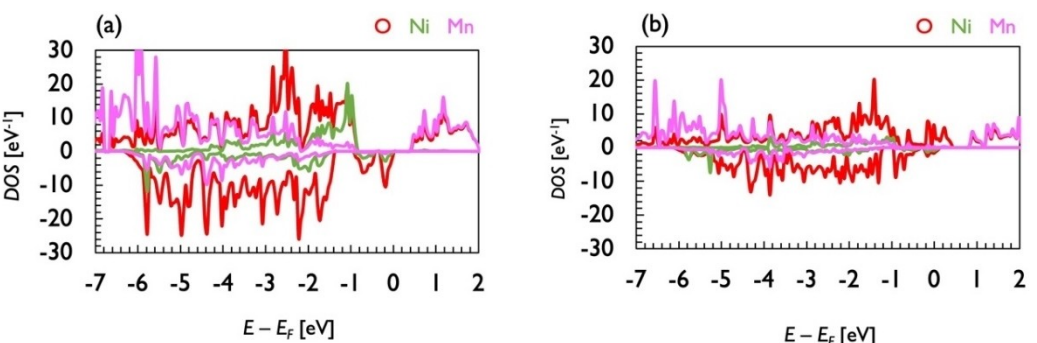


Figure 9. Partial density of state of a) non-defected $\text{Na}_4\text{Mn}_6\text{Ni}_2\text{O}_{20}$ structure and b) 1 Ni atom defected $\text{Na}_4\text{Mn}_6\text{Ni}_1\text{O}_{20}$ structure. Positive and negative values refer to up spin and down spin components, respectively.

performed to obtain the pDOS of metal defected $\text{Na}_4\text{Mn}_6\text{NiO}_{20}$ to clarify which structural defects dominantly facilitate the oxidation of O^{2-} . Figure 9 shows the pDOS of Ni defected structure and non-defected structures in which the atomic positions and cell parameters were optimized.

The structural model used was $2 \times 2 \times 1$ supercell of $\text{Na}_{2/3}(\text{Mn}_{2/3}\text{Ni}_{1/3})\text{O}_2$ unit cell. Considering the non-defected structure, hybrid state of Ni 3d and O 2p orbitals was confirmed at the Fermi level, indicating that the electron was extracted from this Ni 3d-O 2p hybrid orbital. The theoretical results were in good agreement with the experimental results suggesting that Ni ion redox is dominant during electrochemical cycling. On the other hand, the $\text{Na}_4\text{Mn}_6\text{Ni}_1\text{O}_{20}$ which 1 Ni was defected from the $\text{Na}_4\text{Mn}_6\text{Ni}_2\text{O}_{20}$, the electron density of the oxygen at Fermi level was more significant and the electron density of Ni orbital shifted to the lower level than that of non-defected structure. Thus, the hole generated on charge would localize on the oxygen 2p orbital rather than the 3d orbital of TM suggesting that the contribution of oxygen redox for charge compensation increased in defected structure. As reported by several groups, the defects at TM site in layered oxides unlock the oxygen redox since the Na–O–□ configurations (where □ represents vacancy) forms lone pair electron at 2p orbitals that promotes the oxygen redox.^[10,12] Therefore, the oxygen redox was confirmed in the milled sample owing to the defects at Ni sites through mechanical milling. The electron density at Ni 3d orbital still present at the Fermi level, indicates that the Ni ion contributes towards the redox as observed by Ni L-edge XAS. Besides, in the case of Ni defected structure, a hole was formed on the O 2p orbital which was not hybridized with 3d orbital of TM, owing to the Ni defects as demonstrated by the O K-edge XAS. Despite the fact that we showed the results of one Ni defected model, there are the 2 types of Ni and 6 types of Mn defect models based on their structural symmetry, but all the results of other defects model showed similar trends. Furthermore, the metal defects, regardless of the elements and sites, tend to raise the energy level to the electron density of oxygen at Fermi level as shown in Figure S6.

Conclusion

In this study, we investigated the effect of crystallinity of the $\text{Na}_{2/3}(\text{Mn}_{2/3}\text{Ni}_{1/3})\text{O}_2$ with the P2-type layered oxide on the electrochemical properties. The crystallinity of $\text{Na}_{2/3}(\text{Mn}_{2/3}\text{Ni}_{1/3})\text{O}_2$ sample was changed by ball milling. The milled $\text{Na}_{2/3}(\text{Mn}_{2/3}\text{Ni}_{1/3})\text{O}_2$ sample showed better cycling performance compared to that of as-sintered P2-ordered $\text{Na}_{2/3}(\text{Mn}_{2/3}\text{Ni}_{1/3})\text{O}_2$ sample. In addition, the ball milling introduced large amounts of structural defects, such as grain boundary and disordering of layer structure, which further suppressed the P2–O2 structural changes resulting in good cycling performance. The milled samples contain some number of vacancies at TM sites, which were responsible for changing the redox behavior of $\text{Na}_{2/3}(\text{Mn}_{2/3}\text{Ni}_{1/3})\text{O}_2$. Ni ion was dominantly the redox center in the sintered $\text{Na}_{2/3}(\text{Mn}_{2/3}\text{Ni}_{1/3})\text{O}_2$; however, oxide ion also contributes to the charge compensation for the milled $\text{Na}_{2/3}(\text{Mn}_{2/3}\text{Ni}_{1/3})\text{O}_2$ along with Ni ion. Changing the crystallinity has not been intensively investigated for layered oxide materials containing Na thus far, but we consider that it would be an effective approach to improve the electrochemical performance.

Experimental Section

Sample preparation

Sodium hydroxide (NaOH , 99%), nickel hydroxide (Ni(OH)_2 , 99%) and manganese oxide (Mn_2O_3 , 99%) were used as precursors. A mixture of the precursors (2 g) in the metal molar ratio of 2: 2: 1 (Na: Mn: Ni) was ball milled with 50 grams of 4 mm ZrO_2 balls in 80 mL zirconia vials using planetary mixer (Fritsch, P-6) at 500 rpm for 2 h. Subsequently, the milled Na–Mn–Ni mixture was heated at 950 °C for 3 h under air flow and $\text{Na}_{2/3}(\text{Mn}_{2/3}\text{Ni}_{1/3})\text{O}_2$ with P2-type layered structure was obtained. The as-sintered sample was taken out from the furnace at 300 °C and transferred to a dry-box to avoid reaction with moisture. Subsequently, the P2-type layered $\text{Na}_{2/3}(\text{Mn}_{2/3}\text{Ni}_{1/3})\text{O}_2$ sample was further milled at 500 rpm, for 2–10 h, to yield milled samples. One gram of the milled sample was loaded in a zirconia pot (80 mL inner volume) containing several hundred of zirconia balls (4 mm diameter, total mass 40 g). In order to avoid any reaction with water, both the as-sintered and milled samples were handled in a dry-box with a dew point of less than –60 °C.

Characterization

The constituent phases of the samples were identified by X-ray diffraction (XRD, Rigaku, Ultima-IV, Cu-K α). The metal ratio of the as-prepared and charged samples were analyzed using inductively-coupled plasma (ICP) (Shimadzu ICPS-8100). Synchrotron radiation X-ray total scattering experiments were conducted to obtain atomic pair distribution functions (PDFs) using a diffractometer installed at the BL22XU beamline at SPring-8. The sample powders were loaded in pouched cell which is originally designed for in situ X-ray total scattering method, Figure S1. The total scattering data were collected using a flat panel X-ray detector (XRD1621, PerkinElmer) at room temperature with an X-ray energy of 69.35 keV ($\lambda = 0.0178804$ nm). The 2D data were converted into 1D scattering data using the PIXIA program^[32] and the maximum Q range of the obtained total scattering profile reaches approximately 255 nm $^{-1}$. The obtained 1D scattering data were converted into reduced PDFs, G(r), using the Materials PDF program.^[32] The local structures and electron states of Mn and Ni in the sample were examined by Mn and Ni K-edge XAS using synchrotron radiation (BL14B2, SPring-8). The electron states of Mn and Ni were also examined by Mn and Ni L-edge together with O K-edge XAS in partial fluorescence yield mode using synchrotron radiation (BL11, Rits SR center). The obtained XAS data was processed using Demeter package program.^[33] TEM observation was performed using the FEI TITAN3 G2 60-300 instrument operated at an acceleration voltage of 300 kV.

Electrochemical properties

The Na insertion and extraction properties of the samples were evaluated by assembling a two-electrode setup in an IEC R2032 coin-type cell. The working electrodes were prepared by mixing the composites as active materials, Ketjen black as the conductive additive and polytetrafluoroethylene (PTFE) as the binder in the weight ratio of 84:8:8 along with adding a few drops of hexane to facilitate mixing. The mixture was attached to an Al mesh current collector ($\phi = 16$ mm) and heated at 220 °C for 10 h under vacuum to thoroughly remove hexane and water residues. The amount of the composite in each electrode was ca. 10 mg. A lump of metallic Na (Sigma Aldrich) was pressed into a foil and punched out to form the counter electrode ($\phi = 12$ mm, ca.=40 mg) providing twenty times excess amount of Na to serve as a reservoir for the working electrode. A 1.0 mol L $^{-1}$ NaPF₆ solution in ethylene carbonate/diethyl carbonate (EC/DEC, 1:1 by volume, Kishida), and a glass filter (Advantec, GA-100) were used as electrolyte and separator, respectively.

The cell was galvanostatically charged and discharged using a BLS5500 (Keisokuki Center) with a current density of 10 mA g $^{-1}$, in which the denominator represents the mass of the active material in the positive electrode. The other conditions for electrochemical measurement, such as the cut-off potentials, among others have been specified in the Results and Discussion section.

Theoretical calculation

The change in the partial density of state (pDOS) of Na containing layered Ni–Mn oxides, by introducing a defect at TM site was studied using density functional theory (DFT) calculations. The P2-type Na₄Mn₆Ni₂O₂₀ and Na₄Mn₆NiO₂₀ were used for the model cell. Although the molar ratios of the model cells differ from that of the sample investigated in this study, we consider this would not hinder the qualitative discussions regarding the effect of metal defects on the pDOS of the P2 layered oxides. The generalized gradient approximation formula by Perdew, Burke, and Ernzerhof^[34]

was used for the exchange-correlation functional. The projector augmented wave function scheme^[35,36] was employed for treating the core electrons; the valence electrons of Na, Mn, Ni and O were 1, 7, 10 and 6, respectively. The cut-off energy of the wave function was set to 450 eV. Ferri magnetic spin configuration was used for calculation, where the spin orientations of Mn and Ni were antiparallel. To calculate the spin configuration, the repulsion of d electrons were corrected by DFT+U scheme.^[37] The on-site Coulomb parameters for d electrons on the Ni and Mn were 4.0 and 5.0 eV, respectively. The structural model was optimized through the following procedure: firstly, the atomic positions were optimized with the lattice parameters set to experimental values. Subsequently, the lattice parameters were optimized using the optimized atomic positions values. All DFT calculations were performed using the Vienna Ab initio simulation package.^[38-41]

Associated Content Supporting Information

Details on the Structural parameters for Rietveld refinement, results of Rietveld refinement and the results of DFT calculations.

Acknowledgements

Authors thank H. Ofuchi of the Japan Synchrotron Radiation Research Institute (JASRI) for SR hard-XAFS measurements performed at BL14B2 of SPring-8 with the approval of JASRI (Proposal No. 2022 A2015). Authors also thank D. Shibata of the Ritsumeikan Synchrotron Radiation Center for soft-XAFS measurements performed at the SR center of Ritsumeikan University (Proposal No. S22001). The synchrotron total X-ray scattering experiments were performed at BL22XU of SPring-8 with the approval of JASRI (Proposal No. 2022 A3781) and supported by the QST Advanced Research Infrastructure for Materials and Nanotechnology under the remit of "Advanced Research Infrastructure for Materials and Nanotechnology" of the Ministry of Education, Culture, Sports and Technology, Japan, (Proposal No. JPMXP1222QS0013). DFT calculations described in this work were carried out using the computer facilities at the Research Institute for Information Technology, Kyushu University. In addition, the calculations were also conducted in part under the auspices of the Japan Society for the Promotion of Science (JSPS KAKENHI Grant Numbers JP20 K15177).

Conflict of Interest

The authors declare no conflict of interest.

Data Availability Statement

The data that support the findings of this study are available from the corresponding author upon reasonable request.

Keywords: crystallinity · electrochemical activity · P2-type layered oxide material · sodium-ion battery · transitions metal

- [1] C. Delmas, C. Fouassier, P. Hagenmuller, *Physica B+C* **1980**, *99*, 81–85.
- [2] H. Wang, B. Yang, X.-Z. Liao, J. Xu, D. Yang, Y.-S. He, Z. F. Ma, *Electrochim. Acta* **2013**, *113*, 200–204.
- [3] M. Armand, P. Axmann, D. Bresser, M. Copley, K. Edström, C. Ekberg, D. Guyomard, B. Lestriez, P. Novak, M. Petranikova, W. Porcher, S. Trabesinger, M. Wohlfahrt-Mehrens, H. Zhang, *J. Power Sources* **2020**, *479*, 228708.
- [4] R. J. Clement, J. Billaud, A. R. Armstrong, G. Singh, T. Rojo, P. G. Bruce, C. P. Grey, *Energy Environ. Sci.* **2016**, *9*, 3240–3251.
- [5] S. Kumakura, Y. Tahara, S. Sato, K. Kubota, S. Komaba, *Chem. Mater.* **2017**, *29*, 8958–8962.
- [6] H. Yoshida, N. Yabuuchi, K. Kubota, I. Ikeuchi, A. Garsuch, M. Schulz-Dobrick, S. Komaba, *Chem. Commun.* **2014**, *50*, 3677–3680.
- [7] J. Xu, D. H. Lee, R. J. Clement, X. Yu, M. Leskes, A. J. Pell, G. Pintacuda, X.-Q. Yang, C. P. Grey, Y. S. Meng, *Chem. Mater.* **2014**, *26*(2), 1260–1269.
- [8] P. F. Wang, Y. You, Y.-X. Yin, Y.-S. Wang, L.-J. Wan, L. Gu, G. Yu-Guo, *Angew. Chem. Int. Ed.* **2016**, *55*, 7445–7449; *Angew. Chem.* **2016**, *128*, 7571–7575.
- [9] U. Maitra, R. A. House, J. W. Somerville, N. Tapia-Ruiz, J. G. Lozano, N. Guerrini, R. Hao, K. Luo, L. Jin, M. A. Pérez-Osorio, F. Massel, D. M. Pickup, S. Ramos, X. Lu, D. E. McNally, A. V. Chadwick, F. Giustino, T. Schmitt, L. C. Duda, M. R. Roberts, P. G. Bruce, *Nat. Chem.* **2018**, *10*(3), 288–295.
- [10] B. Mortemard de Boisse, S.-i. Nishimura, E. Watanabe, L. Lander, A. Tsuchimoto, J. Kikkawa, E. Kobayashi, D. Asakura, M. Okubo, A. Yamada, *Adv. Energy Mater.* **2018**, *8*, 1800409.
- [11] X. Rong, E. Hu, Y. Lu, F. Meng, C. Zhao, X. Wang, Q. Zhang, X. Yu, L. Gu, Y.-S. Hu, H. Li, X. Huang, X.-Q. Yang, C. Delmas, L. Chen, *Joule* **2019**, *3*, 503–517.
- [12] X.-L. Li, T. Wang, Y. Yuan, X. Y. Yue, Q.-C. Wang, J.-Y. Wang, J. Zhong, R.-Q. Lin, Y. Yao, X.-J. Wu, Y. Xi-Qian, Z. W. Fu, Y.-Y. Xia, X.-Q. Yang, Tongchao Liu, K. Amine, Z. Shadike, Y.-N. Zhou, J. Lu, *Adv. Mater.* **2021**, *33*, 2008194.
- [13] B. Hu, Q. Qiu, C. Li, M. Shen, B. Hu, W. Tong, K. Wang, Q. Zhou, Y. Zhang, Z. He, T. Zhang, C. Chen, *ACS Appl. Mater. Interfaces* **2022**, *14*, 28738–28747.
- [14] C. Zhao, C. Chen, B. Hu, W. Tong, H. Liu, B. Hu, C. Li, *Chem. Mater.* **2022**, *34*, 9240–9250.
- [15] Q. Shi, R. Qi, X. Feng, J. Wang, Y. Li, Z. Yao, Q. Li, X. Lu, J. Zhang, Y. Zhao, *Nat. Comm.* **2022**, *13*, 3205.
- [16] S. F. Linnell, E. J. Kim, Y.-S. Choi, M. Hirsbrunner, S. Imada, A. Pramanik, A. F. Cuesta, D. N. Miller, E. Fusco, B. E. Bode, J. T. S. Irvine, L. C. Duda, D. O. Scanlon, A. R. Armstrong, *J. Mater. Chem. A* **2022**, *10*, 9941–9953.
- [17] C. Zhao, H. Liu, F. Geng, B. Hu, C. Li, *Energy Storage Mater.* **2022**, *48*, 290–296.
- [18] S. Kawasaki, T. Yamanaka, S. Kume, T. Ashida, *Solid State Commun.* **1990**, *76*, 527–530.
- [19] Y. Tsuchiya, A. M. Glushenkov, N. Yabuuchi, *ACS Appl. Nano Mater.* **2018**, *1*, 364–370.
- [20] M. N. Obrovac, O. Mao, J. R. Dahn, *Solid State Ionics* **1998**, *112*, 9–19.
- [21] R. Kataoka, N. Taguchi, T. Kojima, N. Takeichi, T. Kiyobayashi, *J. Mater. Chem. A* **2019**, *7*, 5381–5390.
- [22] T. Sato, K. Sato, W. Zhao, Y. Kajiya, N. Yabuuchi, *J. Mater. Chem. A* **2018**, *6*, 13943–13951.
- [23] P. Strobel, B. Lambert-Andron, *J. Solid State Chem.* **1988**, *75*, 90–98.
- [24] Z. Lu, J. R. Dahn, *J. Electrochem. Soc.* **2001**, *148*, A1225.
- [25] D. H. Lee, J. Xu, Y. S. Meng, *Phys. Chem. Chem. Phys.* **2013**, *15*, 3304–3312.
- [26] L. Yang, X. Li, J. Liu, S. Xiong, X. Ma, P. Liu, J. Bai, W. Xu, Y. Tang, Y.-Y. Hu, M. Liu, H. Chen, *J. Am. Chem. Soc.* **2019**, *141*, 6680–6689.
- [27] Y. Zhang, M. Wu, J. Ma, Guangfeng Wei, Y. Ling, R. Zhang, Y. Huang, *ACS Cent. Sci.* **2020**, *6*, 232–240.
- [28] Q. Liu, Z. Hu, M. Chen, C. Zou, H. Jin, S. Wang, S. Chou, Y. Liu, S. Dou, *Adv. Funct. Mater.* **2020**, *30*, 1909530.
- [29] R. Kataoka, T. Kojima, N. Takeichi, *J. Electrochem. Soc.* **2018**, *165*, A291–A296.
- [30] R. Qiao, L. A. Wray, J. H. Kim, N. P. W. Pieczonka, S. J. Harris, W. Yang, *J. Phys. Chem. C* **2015**, *119*, 27228–27233.
- [31] F. M. F. de Groot, M. Grioni, J. C. Fuggle, J. Ghijssen, G. A. Sawatzky, H. Petersen, *Phys. Rev. B Condens. Matter* **1989**, *40*, 5715–5723.
- [32] S. Tominaka, H. Yamada, S. Hiroi, S. I. Kawaguchi, K. Ohara, *ACS Omega* **2018**, *3*, 8874–8881.
- [33] B. Ravel, M. Newville, *J. Synchrotron Radiat.* **2005**, *12*, 537–541.
- [34] J. P. Perdew, K. Burke, M. Ernzerhof, *Phys. Rev. Lett.* **1996**, *77*, 3865–3868.
- [35] P. E. Blöchl, *Phys. Rev. B* **1994**, *50*, 17953–17979.
- [36] G. Kresse, D. Joubert, *Phys. Rev. B* **1999**, *59*, 1758–1775.
- [37] S. L. Dudarev, G. A. Botton, S. Y. Savrasov, C. J. Humphreys, A. P. Sutton, *Phys. Rev. B* **1998**, *57*, 1505–1509.
- [38] G. Kresse, J. Hafner, *Phys. Rev. B Condens. Matter* **1993**, *47*, 558–561.
- [39] G. Kresse, J. Hafner, *Phys. Rev. B Condens. Matter* **1994**, *49*, 14251–14269.
- [40] G. Kresse, J. Furthmüller, *Comput. Mater. Sci.* **1996**, *6*, 15–50.
- [41] G. Kresse, J. Furthmüller, *Phys. Rev. B* **1996**, *54*, 11169–11186.

Manuscript received: October 21, 2022

Revised manuscript received: November 29, 2022

Accepted manuscript online: December 1, 2022

Version of record online: December 13, 2022